INSTITUTE OF PHYSICS PUBLISHING PHYSICS IN MEDICINE AND BIOLOGY

Phys. Med. Biol. **50** (2005) 4913–4930 doi:10.1088/0031-9155/50/20/011

Coupled radiative transfer equation and diffusion approximation model for photon migration in turbid medium with low-scattering and non-scattering regions

Tanja Tarvainen[1], Marko Vauhkonen[1], Ville Kolehmainen[1], Simon R Arridge[2] and Jari P Kaipio[1]

[1] Department of Applied Physics, University of Kuopio, PO Box 1627, FIN-70211 Kuopio, Finland
[2] Department of Computer Science, University College London, Gower Street, London WC1E 6BT, UK

E-mail: Tanja.Tarvainen@uku.fi

Received 20 June 2005, in final form 15 August 2005
Published 5 October 2005
Online at stacks.iop.org/PMB/50/4913

Abstract

In this paper, a coupled radiative transfer equation and diffusion approximation model is extended for light propagation in turbid medium with low-scattering and non-scattering regions. The light propagation is modelled with the radiative transfer equation in sub-domains in which the assumptions of the diffusion approximation are not valid. The diffusion approximation is used elsewhere in the domain. The two equations are coupled through their boundary conditions and they are solved simultaneously using the finite element method. The streamline diffusion modification is used to avoid the ray-effect problem in the finite element solution of the radiative transfer equation. The proposed method is tested with simulations. The results of the coupled model are compared with the finite element solutions of the radiative transfer equation and the diffusion approximation and with results of Monte Carlo simulation. The results show that the coupled model can be used to describe photon migration in turbid medium with low-scattering and non-scattering regions more accurately than the conventional diffusion model.

(Some figures in this article are in colour only in the electronic version)

1. Introduction

Diffuse optical tomography (DOT) is a relatively new non-invasive imaging method in which images of the optical properties within turbid medium are derived on the basis of measurements

of visible or near-infrared light on the surface of the object (Arridge 1999). It has potential applications in medical imaging, for example in breast cancer detection, monitoring of infant brain tissue oxygenation level and functional brain activation studies; for a recent review see Gibson *et al* (2005).

Image reconstruction in DOT is a nonlinear ill-posed inverse problem. There are no direct methods for the solution of this problem, and thus it is typically stated as a minimization problem such as regularized output least squares. The iterative solution of this problem requires repetitive solutions of the forward problem. Therefore, it is essential to have a computationally feasible forward model that describes light propagation in the medium accurately.

The radiative transfer equation (RTE) is widely accepted as an accurate model for photon migration in turbid medium (Arridge 1999). The RTE does not have analytical solutions for arbitrary geometries, and the numerical solutions with sufficiently dense discretizations lead to computationally demanding problems. Therefore, the RTE has been used as a forward model only in few applications of DOT (Dorn 1998, Klose *et al* 2002).

Due to the computationally intensive nature of the RTE problem, the typical approach in DOT has been to derive approximate, computationally less demanding models based on the RTE. The most typical approach has been to use the diffusion approximation (DA) to the RTE as the forward model. The DA is basically a special case of the first-order spherical harmonics approximation to the RTE, and thus it has some limitations. Firstly, the medium must be scattering dominated, and secondly, light propagation cannot be modelled accurately in the proximity of the collimated light sources and boundaries (Arridge 1999). Due to these limitations, the DA fails to produce accurate estimates for light propagation in the proximity of the source and boundaries, and in the cases in which the turbid medium contains low-scattering or non-scattering regions (Wang and Jacques 1993, Arridge *et al* 2000, Hayashi *et al* 2003). These limitations of the DA can lead to large errors in the reconstructed images; see, e.g., Dehghani *et al* (2000). In medical applications of DOT, a typical low-scattering region is the cerebrospinal fluid layer around the brain.

To overcome the limitations of diffusion theory in the proximity of the light sources, hybrid methods which combine Monte Carlo simulation with diffusion theory have been reported (Wang and Jacques 1993, Alexandrakis *et al* 2000). Monte Carlo is known to describe light propagation accurately. However, it has the disadvantage of requiring a long computation time. Moreover, the hybrid Monte Carlo-diffusion methods often require iterative mapping between the models which increases computation times even more. The hybrid radiative transfer-diffusion approach (Tarvainen *et al* 2005a) can be used to describe light propagation accurately in the proximity of the sources and within turbid medium, but it does not describe photon migration accurately within low-scattering or non-scattering regions. The Focker–Planck equation, which has been found to describe light propagation accurately when the scattering is strongly peaked in the forward direction, can be utilized at the small depths below highly collimated light sources (Kim and Keller 2003). However, it does not describe light propagation accurately at greater depths in biological tissues nor within low-scattering or non-scattering regions.

The radiosity-diffusion model (Arridge *et al* 2000, Dehghani *et al* 2000) has been applied for turbid media with non-scattering regions. However, it does not model light propagation accurately in low-scattering regions or in the proximity of the collimated light sources. Methods that combine Monte Carlo simulation with diffusion theory have also been applied for media with low-scattering and non-scattering regions (Hayashi *et al* 2003). However, also in this case, the approach suffers from the time-consuming nature of the Monte Carlo methods. The coupled transport and diffusion model (Bal and Maday 2002) is also an iterative method which can be utilized in media which contains strongly absorbing and low-scattering regions.

A coupled radiative transfer equation and diffusion approximation model was proposed by the authors in a previous paper (Tarvainen *et al* 2005b) to describe light propagation in turbid medium containing highly collimated light sources. In this paper, the coupled model is extended to take into account low-scattering and non-scattering regions. In this approach, the RTE is used as a forward model in sub-domains in which the assumptions of the DA are not valid. This includes the regions in the proximity of the source and boundary and the low-scattering and non-scattering regions. The DA is used as a forward model elsewhere in the domain. The RTE and DA are coupled through boundary conditions between the RTE and DA sub-domains and they are solved simultaneously using the finite element method (FEM). In the finite element (FE) solution of the RTE in low-scattering or non-scattering regions, the ray-effect may become visible (Lathrop 1968, 1971). Therefore, the streamline diffusion modification is utilized in the FE-solution of the coupled RTE–DA model. The coupled RTE–DA model is designed to overcome the limitations of diffusion theory. It can describe photon migration almost with the same accuracy as the RTE but with less computational burden.

The rest of the paper is organized as follows. The light transport models are described in section 2 and the corresponding numerical methods are given in section 3. The results of the two-dimensional example cases are shown in section 4, and finally, conclusions are given in section 5.

2. Light transport models

2.1. The radiative transfer equation

Let $\Omega \subset \mathbb{R}^n, n = 2$ or 3 denote the physical domain which is considered isotropic in the sense that the probability of scattering between two directions depends only on the relative angle between those directions, not on an absolute direction. Furthermore, let $\partial\Omega$ denote the boundary of the domain and $\hat{s} \in S^{n-1}$ denote a unit vector in the direction of interest. The radiative transfer equation treats photons as particles which undergo elastic collisions until they are absorbed or leave the domain, ignoring the wave nature of light. The frequency domain version of the RTE is of the form

$$\left(\frac{\mathrm{i}\omega}{c} + \hat{s}\cdot\nabla + \mu_\mathrm{s} + \mu_\mathrm{a}\right)\phi(r,\hat{s}) = \mu_\mathrm{s}\int_{S^{n-1}} \phi(r,\hat{s}')\Theta(\hat{s}\cdot\hat{s}')\,\mathrm{d}\hat{s}' + q(r,\hat{s}) \qquad (1)$$

where i is the imaginary unit, ω is the angular modulation frequency of the input signal, c is the speed of light in the medium, μ_s and μ_a are the scattering and absorption coefficients of the medium, respectively, $\phi(r,\hat{s})$ is the radiance, and $q(r,\hat{s})$ is the source inside Ω (Arridge 1999). The kernel $\Theta(\hat{s}\cdot\hat{s}')$ is the scattering phase function which describes the probability that a photon with an initial direction $\hat{s}'$ will have a direction $\hat{s}$ after a scattering event. In DOT, the most usual phase function for isotropic material is the Henyey–Greenstein scattering function (Henyey and Greenstein 1941) which in a three-dimensional (3D) case is of the form

$$\Theta(\hat{s}\cdot\hat{s}') = \frac{1}{4\pi}\frac{1-g^2}{(1+g^2-2g\cos\gamma)^{3/2}} \qquad (2)$$

and in a two-dimensional (2D) case is of the form

$$\Theta(\hat{s}\cdot\hat{s}') = \frac{1}{2\pi}\frac{1-g^2}{(1+g^2-2g\cos\gamma)}. \qquad (3)$$

In equations (2) and (3), γ is the angle between the directions $\hat{s}'$ and $\hat{s}$. The scattering shape parameter g defines the shape of the probability density and it gets values between $-1 < g < 1$. With the value $g = 0$, the scattering probability density is a uniform distribution. For forward dominated scattering $g > 0$ and for backward dominated scattering $g < 0$.

In DOT, we use the boundary condition for the RTE which assumes that no photons travel in an inward direction at the boundary $\partial\Omega$ except at source locations, thus

$$\phi(r,\hat{s}) = \begin{cases} \phi_0(r,\hat{s}), & r \in \cup_j \varepsilon_j, \quad \hat{s}\cdot\hat{n} < 0 \\ 0, & r \in \partial\Omega \backslash \cup_j \varepsilon_j, \quad \hat{s}\cdot\hat{n} < 0 \end{cases} \tag{4}$$

where $\hat{n}$ is the outward unit normal on $\partial\Omega$ and $\phi_0(r,\hat{s})$ is a boundary source at the source position $\varepsilon_j \subset \partial\Omega$ (Arridge 1999, Tarvainen *et al* 2005a).

In the case of DOT, the measurable quantity is the exitance $X(r)$ on the boundary of the domain. It is defined as (Arridge and Hebden 1997)

$$X(r) = \int_{S^{n-1}} \phi(r,\hat{s})(\hat{s}\cdot\hat{n})\,\mathrm{d}\hat{s}. \tag{5}$$

Another quantity of interest is the photon density $\Phi(r)$ which is of the form

$$\Phi(r) = \int_{S^{n-1}} \phi(r,\hat{s})\,\mathrm{d}\hat{s}. \tag{6}$$

2.2. The diffusion approximation

In DOT, the light propagation in tissues is usually modelled with the diffusion approximation to the RTE. In the diffusion approximation framework, the approximation that is used for the radiance is of the form

$$\phi(r,\hat{s}) \approx \frac{1}{|S^{n-1}|}\Phi(r) - \frac{n}{|S^{n-1}|}\hat{s}\cdot(\kappa\nabla\Phi(r)) \tag{7}$$

where n is the dimension of the domain ($n = 2, 3$). The parameter $\kappa = (n(\mu_\mathrm{a} + \mu_\mathrm{s}'))^{-1}$ is the diffusion coefficient where $\mu_\mathrm{s}' = (1 - g_1)\mu_\mathrm{s}$ is the reduced scattering coefficient, and g_1 is the mean of the cosine of the scattering angle (Arridge 1999, Heino and Somersalo 2002, Kaipio and Somersalo 2005). In the case of the Henyey–Greenstein scattering function, equations (2) and (3), we have $g_1 = g$. The DA is basically a first-order angular approximation for the RTE. Therefore it has some limitations. Firstly, the medium must be scattering dominated, and secondly, light propagation cannot be modelled accurately in the proximity of the collimated light sources and boundaries. The frequency domain version of the DA is of the form

$$-\nabla\cdot\kappa\nabla\Phi(r) + \mu_\mathrm{a}\Phi(r) + \frac{\mathrm{i}\omega}{c}\Phi(r) = q_0(r) \tag{8}$$

where $q_0(r)$ is the source inside Ω.

The diffusion approximation cannot satisfy the boundary condition (4). Instead it is often replaced by an approximation that the total inward directed photon current is zero. Further, by taking into account the mismatch between the refractive indices of the medium and surrounding medium, a Robin-type boundary condition can be derived. It is of the form

$$\Phi(r) + \frac{1}{2\gamma_n}\kappa A\frac{\partial\Phi(r)}{\partial\hat{n}} = 0, \qquad r \in \partial\Omega \tag{9}$$

where γ_n is a dimension-dependent constant which takes the values $\gamma_2 = 1/\pi$ and $\gamma_3 = 1/4$ and A is a parameter governing the internal reflection at the boundary $\partial\Omega$ (Arridge 1999, Kaipio and Somersalo 2005), with $A = 1$ for the case of matched refractive index.

The light sources at $\partial\Omega$ are usually modelled in the DA either by the collimated source model or the diffuse boundary source model. In the case of the collimated source model, the light source is modelled as an isotropic point source located at a depth $1/\mu_\mathrm{s}'$ below the source site (Schweiger *et al* 1995). In the case of the diffuse boundary source model, the source is modelled as a diffuse boundary current at the source position $\varepsilon_j \subset \partial\Omega$ (Schweiger *et al* 1995).

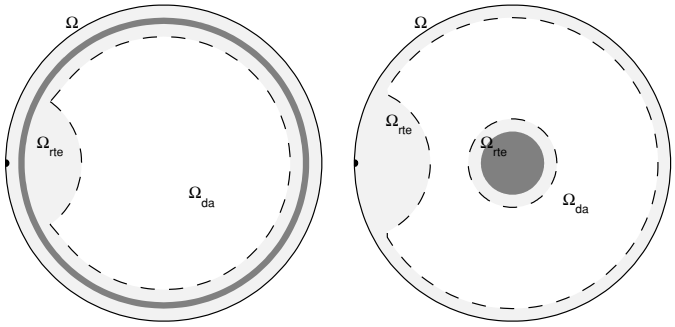

Figure 1. Two examples of domain Ω with an inclusion (dark grey). On the left, the inclusion is a ring-like gap close to the boundary, and on the right, the inclusion is a hole at the centre. The source is located on the left. The RTE is used as a forward model in the sub-domain Ω_{rte} (light grey colour), the DA is used as a forward model in the sub-domain Ω_{da} (white colour), and the interface Γ separates the RTE and DA sub-domains (dashed line).

The exitance, which is the measurable quantity, can be derived to have the following formulation:

$$X(r) = -\kappa \frac{\partial \Phi(r)}{\partial \hat{n}} = \frac{2\gamma_n}{A} \Phi(r). \tag{10}$$

2.3. The coupled RTE–DA model

Let us now consider a circular domain Ω similar to the example images illustrated in figure 1. The domain contains an inclusion which is a low-scattering or non-scattering region as marked with dark grey colour in the images of figure 1. In the left image, the inclusion is a ring-like gap close to the boundary, and in the right image, the inclusion is a hole at the centre. The refractive index is assumed to be constant within the whole domain, and thus it is assumed that there are no refraction or reflection effects between the background medium and the inclusions.

In the coupled RTE–DA model, the RTE is used as a forward model in sub-domain Ω_{rte} in which the assumptions of the DA are not valid. The sub-domain Ω_{rte} includes the regions in the proximity of the source and boundary and the inclusion, and it is illustrated in figure 1 with light grey colour. The DA is used as a forward model in sub-domain Ω_{da}. The DA sub-domain Ω_{da} includes the remaining domain and it is illustrated in figure 1 with white colour. Let $\partial\Omega_{\mathrm{rte}}$ denote the boundary of the domain Ω_{rte}, and $\partial\Omega_{\mathrm{da}}$ denote the boundary of the domain Ω_{da}. Furthermore, let Γ denote the interface that separates the sub-domains Ω_{rte} and Ω_{da}. In the cases considered in this paper, $\Gamma = \partial\Omega_{\mathrm{da}}$. The interface Γ is marked in the images of figure 1 with a dashed line. We note that the interface Γ should be located within the region in which the assumptions of the DA are valid. Thus, for example in the case of a turbid medium which contains a low-scattering or non-scattering region, Γ should be located inside the highly scattering region. The location of the interface Γ can be, for example, determined by comparing the deviation of the angular distribution of the radiance from the first-order approximation. The location should be chosen such that the angular distribution of the radiance is 'smooth' enough to be well approximated by the first-order approximation. The external boundary $\partial\Omega$ is included into the RTE sub-domain Ω_{rte}, and therefore, we use the following notation $\partial\Omega_{\mathrm{rte,out}} = \partial\Omega_{\mathrm{rte}} \backslash \Gamma$ for the external boundary. The coupled RTE–DA

model is derived by coupling the RTE (1) and the DA (8) on the interface Γ using relations (6) and (7). The coupled RTE–DA model can now be written in the form (Tarvainen *et al* 2005b)

$$\left(\frac{\mathrm{i}\omega}{c} + \hat{s}\cdot\nabla + \mu_\mathrm{s} + \mu_\mathrm{a}\right)\phi(r,\hat{s}) = \mu_\mathrm{s}\int_{S^{n-1}} \phi(r,\hat{s}')\Theta(\hat{s}\cdot\hat{s}')\,\mathrm{d}\hat{s}' + q(r,\hat{s}), \qquad r\in\Omega_\mathrm{rte} \tag{11}$$

$$\phi(r,\hat{s}) = \begin{cases} \phi_0(r,\hat{s}), & r\in\cup_j\varepsilon_j, \quad \hat{s}\cdot\hat{n} < 0 \\ 0, & r\in\partial\Omega_{\mathrm{rte,out}}\setminus\cup_j\varepsilon_j, \quad s\cdot\hat{n} < 0 \end{cases} \tag{12}$$

$$\phi(r,\hat{s}) = \frac{1}{|S^{n-1}|}\Phi(r) - \frac{n}{|S^{n-1}|}\hat{s}\cdot(\kappa\nabla\Phi(r))\,, \qquad r\in\Gamma \tag{13}$$

$$-\nabla\cdot\kappa\nabla\Phi(r) + \mu_\mathrm{a}\Phi(r) + \frac{\mathrm{i}\omega}{c}\Phi(r) = q_0(r), \qquad r\in\Omega_\mathrm{da} \tag{14}$$

$$\Phi(r) = \int_{S^{n-1}} \phi(r,\hat{s})\,\mathrm{d}\hat{s}, \qquad r\in\Gamma \tag{15}$$

where the parameters are as described earlier.

3. Numerical methods

In this study the RTE, the DA and the coupled RTE–DA model are numerically solved using the finite element method. The finite element solutions are compared with the results of Monte Carlo simulation.

3.1. Finite element method

In the finite element method, a variational formulation is derived for the original problem. Then, a finite-dimensional approximation for the variational formulation is constructed using suitably chosen basis and test functions in the solution space.

3.1.1. FE-approximation of the RTE. In this study, the FE-approximation of the RTE is based on the model in Tarvainen *et al* (2005a). Both the spatial and angular discretizations are implemented in piecewise linear bases. Further, the streamline diffusion modification described by Richling *et al* (2001) is applied. The streamline diffusion modification has been found to stabilize FE-solutions in situations in which standard FE-techniques produce oscillating results. One example of such situation is the FE-solution of the RTE in a low-scattering medium, where the ray-effect may become visible. In the streamline diffusion modification, the test function is of the form $(v + \delta\hat{s}\cdot\nabla v)$ instead of the standard method in which the test function is v. The parameter δ is the 'smoothing' parameter which is a spatially varying constant that depends on the local absorption and scattering. In this study, it is chosen as $\delta = \min\left\{\frac{1}{2(\mu_\mathrm{a}+\mu_\mathrm{s})}, \frac{5}{(\mu_\mathrm{a}+\mu_\mathrm{s})r_j}\right\}$, where r_j is the distance from the source.

The FE-approximation of the RTE can be written in the form

$$(A_0 + A_1 + A_2 + A_3 + A_4)\alpha = b\psi^0 \tag{16}$$

where $\alpha = (\alpha_{1,1}, \alpha_{1,2}, \ldots, \alpha_{1,N_\mathrm{a}}, \alpha_{2,1}, \ldots, \alpha_{2,N_\mathrm{a}}, \ldots, \alpha_{N_\mathrm{n},1}\ldots, \alpha_{N_\mathrm{n},N_\mathrm{a}})^T \in \mathbb{C}^{N_\mathrm{n}N_\mathrm{a}}$ is the radiance in nodal points of the spatial and angular meshes, N_n is the number of spatial nodes, and N_a is the number of angular directions. Further, $\psi^0 = \left(\psi^0_{1,1}, \ldots, \psi^0_{N_\mathrm{n},N_\mathrm{a}}\right)^T \in \mathbb{R}^{N_\mathrm{n}N_\mathrm{a}}$ is the source strength vector having nonzero elements for spatial nodes $r_i \in \varepsilon_j \subset \partial\Omega$ such that $\psi^0_{i,\ell}$ is the source power at the node i in the 'direction' ℓ. The components of the matrix

equation (16) are of the form

$$A_0(h,s) = \frac{\mathrm{i}\omega}{c}\left(\int_V \psi_i(r)\psi_j(r)\,\mathrm{d}r \int_{S^{n-1}} \psi_\ell(\hat{s})\psi_m(\hat{s})\,\mathrm{d}\hat{s} + \int_V \delta \int_{S^{n-1}} \hat{s}\cdot\nabla\psi_j(r)\psi_m(\hat{s})\psi_\ell(\hat{s})\,\mathrm{d}\hat{s}\psi_i(r)\,\mathrm{d}r\right) \tag{17}$$

$$A_1(h,s) = -\int_V \int_{S^{n-1}} \hat{s}\cdot\nabla\psi_j(r)\psi_m(\hat{s})\psi_\ell(\hat{s})\,\mathrm{d}\hat{s}\psi_i(r)\,\mathrm{d}r + \int_V \delta \int_{S^{n-1}} (\hat{s}\cdot\nabla\psi_j(r)\psi_m(\hat{s}))(\hat{s}\cdot\nabla\psi_i(r)\psi_\ell(\hat{s}))\,\mathrm{d}\hat{s}\,\mathrm{d}r \tag{18}$$

$$A_2(h,s) = \int_{\partial V} \psi_i(r)\psi_j(r)\,\mathrm{d}S \int_{S^{n-1}} (\hat{s}\cdot\hat{n})_+\psi_\ell(\hat{s})\psi_m(\hat{s})\,\mathrm{d}\hat{s} \tag{19}$$

$$A_3(h,s) = \int_V (\mu_\mathrm{s}+\mu_\mathrm{a})\psi_i(r)\psi_j(r)\,\mathrm{d}r \int_{S^{n-1}} \psi_\ell(\hat{s})\psi_m(\hat{s})\,\mathrm{d}\hat{s} + \int_V \delta(\mu_\mathrm{s}+\mu_\mathrm{a}) \int_{S^{n-1}} \hat{s}\cdot\nabla\psi_j(r)\psi_m(\hat{s})\psi_\ell(\hat{s})\,\mathrm{d}\hat{s}\psi_i(r)\,\mathrm{d}r \tag{20}$$

$$A_4(h,s) = -\int_V \mu_\mathrm{s}\psi_i(r)\psi_j(r)\,\mathrm{d}r \int_{S^{n-1}}\int_{S^{n-1}} \Theta(\hat{s}\cdot\hat{s}')\psi_\ell(\hat{s}')\,\mathrm{d}\hat{s}'\psi_m(\hat{s})\,\mathrm{d}\hat{s} - \int_V \delta\mu_\mathrm{s} \int_{S^{n-1}} \hat{s}\cdot\nabla\psi_j(r)\psi_m(\hat{s}) \int_{S^{n-1}} \Theta(\hat{s}\cdot\hat{s}')\psi_\ell(\hat{s}')\,\mathrm{d}\hat{s}'\mathrm{d}\hat{s}\psi_i(r)\,\mathrm{d}r \tag{21}$$

$$b(h,s) = \int_{\partial V} \psi_i(r)\psi_j(r)\,\mathrm{d}S \int_{S^{n-1}} (\hat{s}\cdot\hat{n})_-\psi_\ell(\hat{s})\psi_m(\hat{s})\,\mathrm{d}\hat{s} \tag{22}$$

where V is the domain Ω and ∂V is its boundary $\partial\Omega$, and $h = N_\mathrm{a}(j-1)+m$, $s = N_\mathrm{a}(i-1)+\ell$ ($j,i = 1,\ldots,N_\mathrm{n}$, $m,\ell = 1,\ldots,N_\mathrm{a}$, $h,s = 1,\ldots,N_\mathrm{n}N_\mathrm{a}$). Further, $\psi_i(r)$, $\psi_\ell(\hat{s})$, $\psi_j(r)$ and $\psi_m(\hat{s})$ are the basis functions and $(\hat{s}\cdot\hat{n})_\pm$ denotes the positive and negative parts of $(\hat{s}\cdot\hat{n})$.

3.1.2. FE-approximation of the DA. The FE-approximation of the DA is of the form

$$(K+C+R+Z)\,a = E \tag{23}$$

where $a = (a_1,\ldots,a_N)^T \in \mathbb{C}^N$ is the photon density in nodal points of the FE-mesh and N is the number of nodal points. The components of the matrix equation (23) are of the form

$$K(p,k) = \int_V \kappa\nabla\varphi_k(r)\cdot\nabla\varphi_p(r)\,\mathrm{d}r \tag{24}$$

$$C(p,k) = \int_V \mu_\mathrm{a}\varphi_k(r)\varphi_p(r)\,\mathrm{d}r \tag{25}$$

$$Z(p,k) = \frac{\mathrm{i}\omega}{c}\int_V \varphi_k(r)\varphi_p(r)\,\mathrm{d}r \tag{26}$$

$$R(p,k) = \int_{\partial V} \frac{2\gamma_n}{A}\varphi_k(r)\varphi_p(r)\,\mathrm{d}S \tag{27}$$

where V is the domain, ∂V is the boundary of the domain, $k,p = 1,\ldots,N$, and $\varphi_k(r)$ and $\varphi_p(r)$ are the basis functions. In this study, the collimated source model is used. Thus, the

source vector E is of the form

$$E(p) = \int_V q_0 \varphi_p(r)\,\mathrm{d}r, \qquad r \in \cup_j \varepsilon_j. \tag{28}$$

For further details, see e.g. Tarvainen *et al* (2005a).

3.1.3. FE-approximation of the coupled RTE–DA model. The FE-approximation of the coupled RTE–DA model is based on the method described by Tarvainen *et al* (2005b), with the streamline diffusion modification (Richling *et al* 2001) being applied. The FE-approximation of the coupled RTE–DA model, equations (11)–(15), can be written in the form

$$\begin{pmatrix} A_{\mathrm{rte}} & D \\ F & A_{\mathrm{da}} \end{pmatrix} \begin{pmatrix} \alpha \\ a \end{pmatrix} = \begin{pmatrix} b_{\mathrm{rte}} \\ 0 \end{pmatrix} \tag{29}$$

where vector α is the radiance in nodal points of the FE-mesh in Ω_{rte} and vector a is the photon density in nodal points of the FE-mesh in Ω_{da}. The components of the matrix equation (29) are of the following form. The block A_{rte} is of the form

$$A_{\mathrm{rte}} = A_0 + A_1 + A_2 + A_3 + A_4 \tag{30}$$

where A_0, A_1, A_2, A_3 and A_4 are as in (17)–(21), where $V = \Omega_{\mathrm{rte}}$ and $\partial V = \partial\Omega_{\mathrm{rte}}$. The block A_{da} is of the form

$$A_{\mathrm{da}} = K + C + Z \tag{31}$$

where K, C and Z are as in (24)–(26), where $V = \Omega_{\mathrm{da}}$. Furthermore, the matrices D and F, which contain the boundary conditions on the interface Γ, are of the form

$$\begin{aligned} D(h,k) = &-\frac{1}{|S^{n-1}|}\int_\Gamma \varphi_k(r)\psi_j(r)\,\mathrm{d}S \int_{S^{n-1}} (\hat{s}\cdot\hat{n})_-\psi_m(\hat{s})\,\mathrm{d}\hat{s} \\ &+ \frac{n}{|S^{n-1}|}\int_\Gamma \kappa \int_{S^{n-1}} (\hat{s}\cdot\hat{n})_- \left(\hat{s}\cdot\nabla\varphi_k(r)\right)\psi_m(\hat{s})\,\mathrm{d}\hat{s}\psi_j(r)\,\mathrm{d}S \end{aligned} \tag{32}$$

$$F(p,s) = -\int_\Gamma \kappa\,(\hat{n}\cdot\nabla\psi_i(r))\,\varphi_p(r)\,\mathrm{d}S \int_{S^{n-1}} \psi_\ell(\hat{s})\,\mathrm{d}\hat{s} \tag{33}$$

where $h = N_{\mathrm{a}}(j-1)+m$, $s = N_{\mathrm{a}}(i-1)+\ell$ ($j, i = 1,\ldots,N_{\mathrm{n}}$, $m, \ell = 1,\ldots,N_{\mathrm{a}}$, $h, s = 1,\ldots,N_{\mathrm{n}}N_{\mathrm{a}}$), and $k, p = 1,\ldots,N$. The source vector $b_{\mathrm{rte}} \in \mathbb{R}^{N_{\mathrm{n}}N_{\mathrm{a}}}$ is of the form $b_{\mathrm{rte}} = b\psi^0$, where ψ^0 is the source strength vector and the matrix b is as in (22), where $\partial V = \partial\Omega_{\mathrm{rte,out}}$.

3.2. Monte Carlo simulation

Monte Carlo is a statistical simulation method in which paths of photons are traced as the photons are scattered and absorbed within the medium. Monte Carlo is known to produce accurate estimates for light propagation in tissues. However, due to its statistical nature, it has the disadvantage of requiring long computation time. Therefore, Monte Carlo is usually used as a reference method for other approaches.

The Monte Carlo code used here is a similar to the anisotropic codes described in Heino *et al* (2003) and Heiskala *et al* (2005). In this study, a 2D situation is considered and the medium is isotropic. The photon packet method (Prahl *et al* 1989) is used. The Monte Carlo code proceeds in the following way. First, a photon packet is launched into the domain at the source position with an initial weight w. The step size L of the photon packet is calculated using exponential probability density function. At each step, a part of the packet is absorbed.

Table 1. The optical properties of the background medium and the inclusion for different tests.

	Background			Inclusion		
	μ_a (mm^{-1})	μ_s (mm^{-1})	g	μ_a (mm^{-1})	μ_s (mm^{-1})	g
A	0.025	2	0	0.025	0.02	0
B	0.025	2	0	0.025	0	–
C	0.025	2	0.8	0.025	0.02	0.9

The absorption is handled by reducing the weight w of the photon packet by $\exp(-\mu_a L)$. After a scattering event, a new direction is calculated using the Henyey–Greenstein scattering function (3). Thus, if the photon direction before the scattering event is $\hat{s}' = (\cos\theta', \sin\theta')$, the new direction $\hat{s} = (\cos\theta, \sin\theta)$ is obtained by

$$\theta = \theta' + \tilde{\theta} \tag{34}$$

where

$$\tilde{\theta} = 2\tan^{-1}\left(\frac{1-g}{1+g}\tan(\pi\xi)\right) \tag{35}$$

where g is the scattering shape parameter as in equation (3), and ξ is a random variable uniformly distributed between zero and one. Thus, if $g = 0$ the scattering angle $\tilde{\theta}$ is obtained from a uniform distribution from 0 to 2π. The photon packet propagation is continued until the packet either escapes the domain or the weight falls below a predefined minimum. If the photon packet escapes the domain, the weight of the packet is saved and contributes to the boundary data (exitance).

4. Results

The performance of the coupled RTE–DA approach was tested with 2D simulations. For comparison, the FE-solutions of the RTE and the DA were computed. The FE-solutions were also compared with the results of Monte Carlo simulation. The finite element calculations and the Monte Carlo simulations were performed as described in section 3. The quantities that were investigated were the photon density inside the domain and the exitance, equations (5) and (10), on the boundary of the domain. Both the photon density within the domain and exitance on the boundary of the domain were obtained from the results of the finite element calculations. As the result of the Monte Carlo simulation, the exitance on the boundary of the domain was obtained.

In simulations, a highly scattering circular domain Ω which contained a low-scattering or non-scattering inclusion was examined. Similar domains are illustrated in the images of figure 1. The radius of the circle was 25 mm and the centre was located at the origin. The collimated light source was located at $(-25\ 0)$ with the direction perpendicular to $\partial\Omega$. The modulation frequency of the input signal was chosen as 50 MHz. The refractive indices of the background medium, inclusion and the surrounding medium were chosen as $n_{in} = 1.4$, and thus the reflection parameter was $A = 1$ when solving the DA in the whole domain. Two types of inclusions were investigated: a ring-like gap close to the boundary and a hole at the centre. Different inclusion sizes were tested as well as different optical properties. The optical properties of the test cases are summarized in table 1.

The finite element solution of the RTE, the coupled RTE–DA model and the DA were computed in the same spatial mesh. In the case of the ring-like gap, the spatial FE-discretization

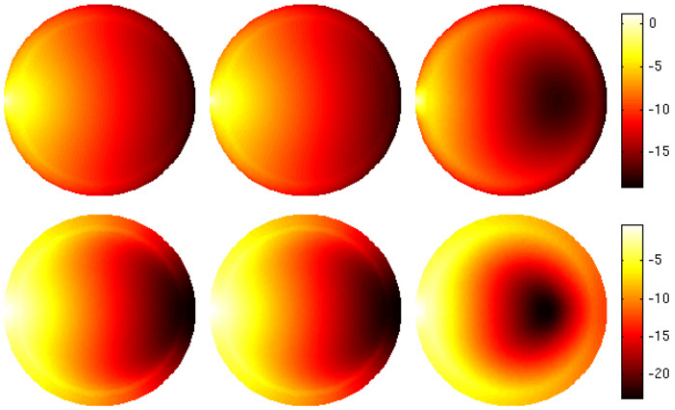

Figure 2. Logarithm of amplitude (top row) and phase shift (bottom row) of photon density within a domain which contained a 1 mm wide low-scattering gap (case 1.A). From left to right: the RTE solution, the coupled RTE–DA solution and the DA solution.

contained 3954 nodal points and 7731 triangular elements. In the case of the hole at the centre, the FE-discretization contained 4134 nodal points and 8046 triangular elements. The angular discretization for the RTE contained 16 (tests A and B) or 32 (test C) directions. In the FE-discretization of the coupled RTE–DA model, the interface Γ which separates the RTE and DA sub-domains is located at a distance 20 mm from the source and 2 mm from the external boundary and the boundary of the inclusion.

4.1. Case 1: ring-like gap

As the first case, we investigated a situation in which the domain contained a ring-like gap close to the boundary (left image of figure 1). The width of the gap was 1 mm and its outer boundary located 3 mm from the boundary. The optical properties of the test cases are summarized in table 1. In all of the test cases, the background absorption and scattering coefficients were $\mu_a = 0.025$ mm^{-1} and $\mu_s = 2$ mm^{-1}, respectively, and the absorption coefficient of the gap was $\mu_a = 0.025$ mm^{-1}. In the first test case (case 1.A), the gap consisted of low-scattering medium with $\mu_s = 0.02$ mm^{-1}. The scattering probability was a uniform distribution, and thus the scattering shape parameters of the background medium and gap were $g = 0$. In the second test case (case 1.B), the gap consisted of non-scattering medium ($\mu_s = 0$ mm^{-1}) and the scattering probability of the background medium was a uniform distribution ($g = 0$). Further, in the third test case (case 1.C), the gap consisted of low-scattering medium and the scattering probability was a non-uniform distribution. The scattering coefficient of the gap was $\mu_s = 0.02$ mm^{-1} and the scattering shape parameters of the background medium and the gap were $g = 0.8$ and $g = 0.9$, respectively.

First, the photon densities inside the domain were investigated. The results of the low-scattering gap test (case 1.A) are shown in figure 2 which shows the photon densities within the domain solved with the RTE, the coupled RTE–DA model and the DA (images from left to right in the respective order). The logarithms of amplitudes are shown on the top row and the phase shifts are shown on the bottom row. The photon densities along the source direction for all of the test cases are shown in figure 3. The logarithms of amplitudes against the distance from the source are shown on the left and the phase shifts against the distance from the source are shown on the right. The images from top to bottom are from the following test cases:

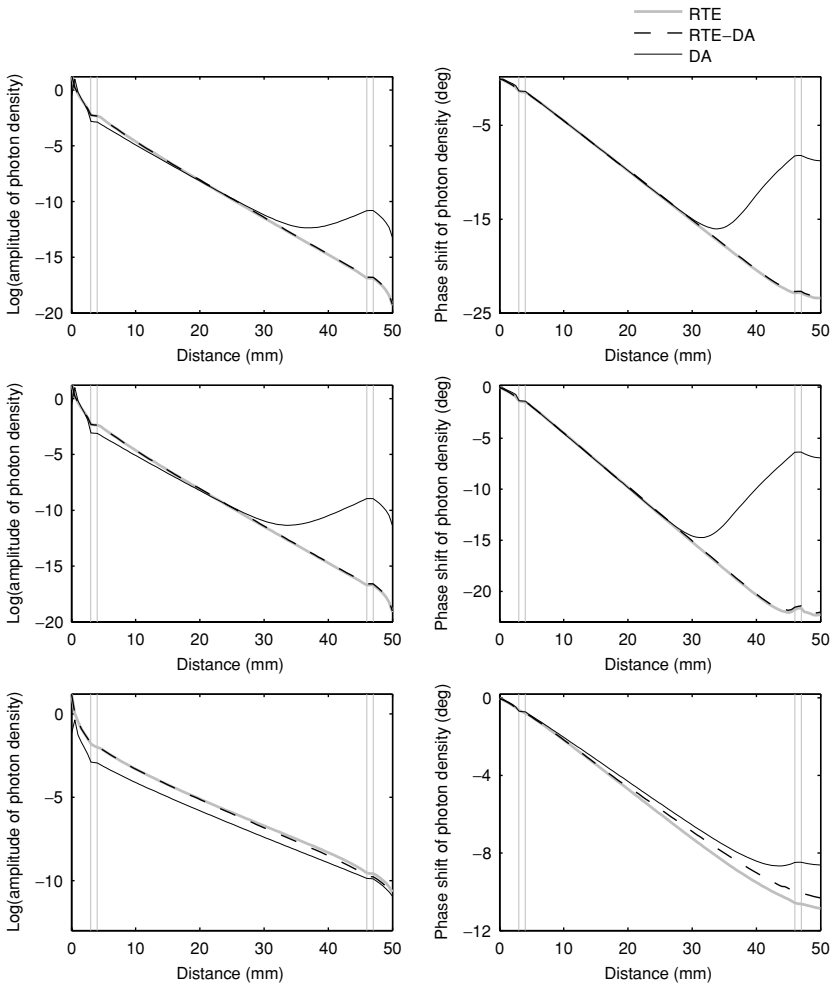

Figure 3. Logarithm of amplitude (left column) and phase shift (right column) of photon density against the distance from source in a domain with a 1 mm wide gap. From top to bottom: a low-scattering gap (case 1.A), a non-scattering gap (case 1.B) and non-uniform scattering (case 1.C). The locations of the gap are marked with thin grey lines.

a low-scattering gap (case 1.A), a non-scattering gap (case 1.B) and non-uniform scattering (case 1.C) where the optical properties are as shown in table 1. The results in figures 2 and 3 are in the same scale. The amplitude data were scaled with respect to the source strength. The phase data do not depend on the source strength and therefore it did not need to be scaled.

The exitance, which is the measurable quantity on the boundary of the domain, was also examined. The exitances that were calculated with the different approaches are shown in figure 4. The logarithms of amplitudes against the detection angle are shown on the left and the phase shifts against the detection angle are shown on the right. The images from top to bottom are from the following test cases: a low-scattering gap (case 1.A), a non-scattering gap (case 1.B) and non-uniform scattering (case 1.C). The results in figure 4 are in the same scale.

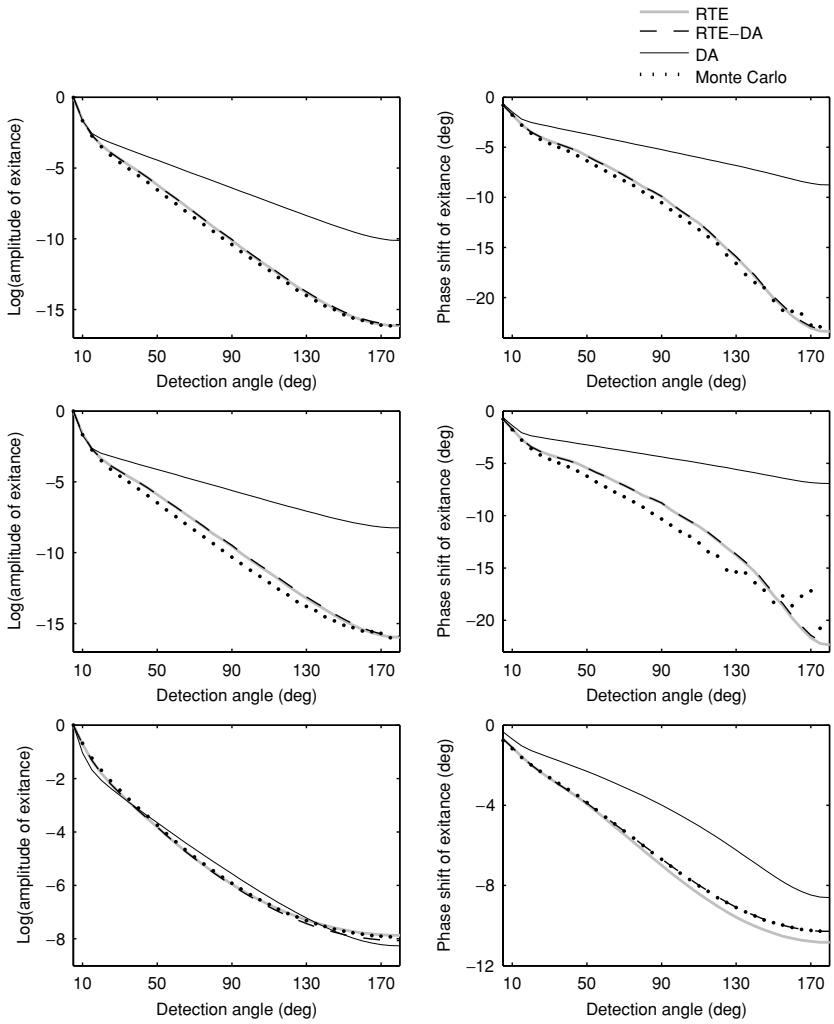

Figure 4. Logarithm of amplitude (left column) and phase shift (right column) of exitance against the detection angle in a domain with a 1 mm wide gap. From top to bottom: a low-scattering gap (case 1.A), a non-scattering gap (case 1.B) and non-uniform scattering (case 1.C).

The amplitude data were scaled with respect to the amplitude of the measurement position closest to the source.

Examining the photon densities within the domain (figures 2 and 3) shows that the proposed coupled RTE–DA model gives almost the same results as the RTE. The photon densities solved with the DA, however, differ clearly from the RTE solution. As can be seen from figure 2, the photon density within the gap is higher than the photon density within the surrounding background medium. Thus, the photons tend to propagate further within the gap. The amplitudes and phase shifts of photon densities obtained with the RTE and the coupled RTE–DA model are almost equal which can be seen from figure 3. All the solutions show almost a flat region in the amplitude and phase data on the location of the gap. The shape of the DA solution, however, differs from the other approaches at this point. According to our tests if the size of the gap is made wider, the flat region widens as well and the

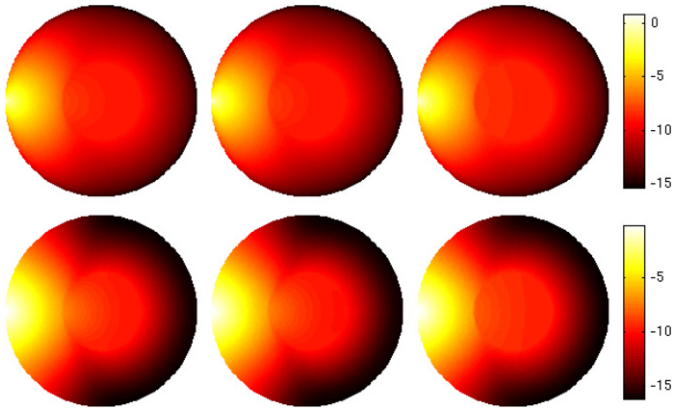

Figure 5. Logarithm of amplitude (top row) and phase shift (bottom row) of photon density within a domain which contained a low-scattering hole with a radius of 10 mm (case 2.A). From left to right: the RTE solution, the coupled RTE–DA solution and the DA solution.

Table 2. FE-matrix sizes, number of nonzero elements and the forward solution computation times for the RTE, the coupled RTE–DA model and the DA in the low-scattering gap test (case 1.A). The number of angular directions in the RTE discretization was 16.

	Matrix size	Nonzeros	Time (s)
RTE	63 264 × 63 264	6994 432	1365.4
RTE–DA	41 799 × 41 799	4381 981	754.1
DA	3 954 × 3 954	27 322	6.4

difference between the DA solution and other approaches increases. As can be seen from figure 3, the DA solution differs clearly from the other approaches especially farther from the source.

Examining the exitances on the boundary of the domain and comparing the FE-solutions with Monte Carlo simulations supports the results. The coupled RTE–DA model and the RTE give almost the same results as Monte Carlo. The DA, however, differs clearly from the Monte Carlo solution. This can be seen from figure 4 in which the logarithms of amplitudes and phase shifts of exitances against the detection angle are shown. The amplitudes and phase shifts solved with the RTE, the coupled RTE–DA and Monte Carlo are almost the same whereas the DA solution differs clearly from the other solutions. The similar 'kink' that was noted by Arridge *et al* (2000) can be seen both in amplitude and phase data of our results as well, and it is located around a detection angle 15°. It was noted that as the width of the gap increases, the location of the 'kink' is displaced.

Information about FE-matrix sizes and number of nonzero elements in them as well as the computation times for the low-scattering gap test (case 1.A) are summarized in table 2. All the FE-solutions were computed using the biconjugate gradient method in Matlab environment. The iterations were proceeded until they converged. As can be seen from table 2, the FE-discretization of the RTE is 16^2 times bigger than FE-discretization of the DA. The coupled RTE–DA model includes both the RTE and DA sub-domains and the size of the FE-discretization depends on the amount and size of the low-scattering and non-scattering regions. As can be seen from table 2, the computation times for the RTE and the coupled RTE–DA model are both longer than for the whole domain DA. However, the coupled

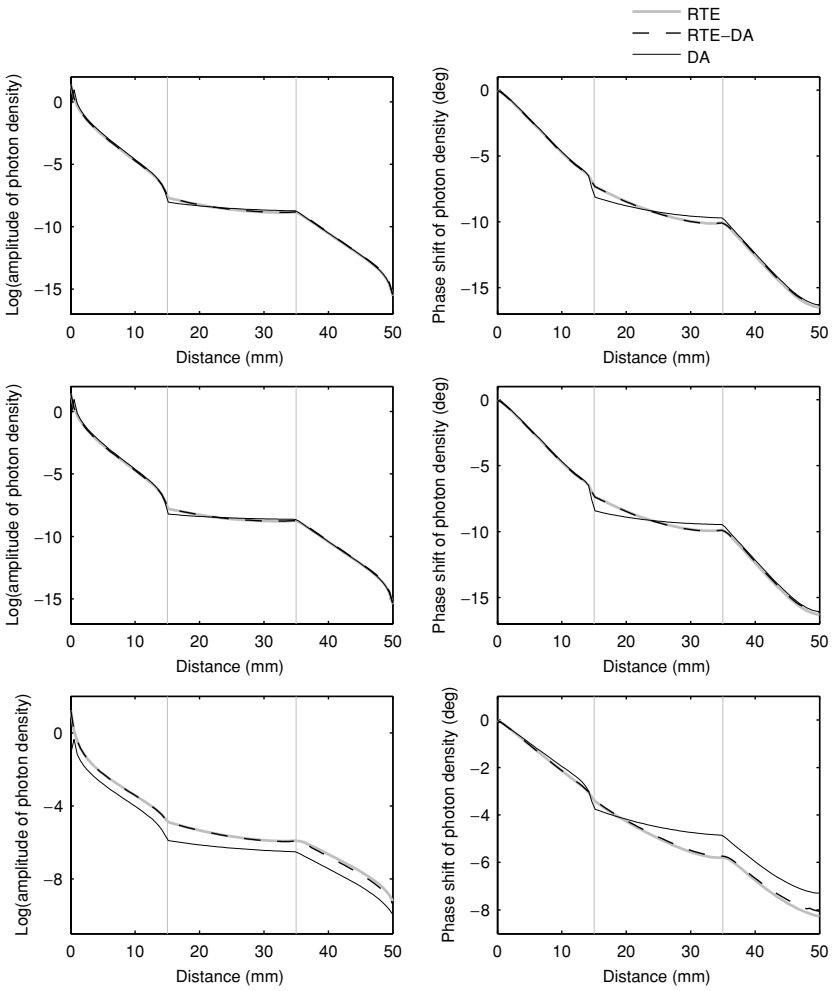

Figure 6. Logarithm of amplitude (left column) and phase shift (right column) of photon density against the distance from the source in a domain with a 10 mm radius hole at the centre. From top to bottom: a low-scattering hole (case 2.A), a non-scattering hole (case 2.B) and non-uniform scattering (case 2.C). The location of the hole is marked with thin grey lines.

RTE–DA solution is obtained almost two times faster than the solution using the RTE in the whole domain.

4.2. Case 2: hole at the centre

As the second case, we investigated a situation in which the domain contained a hole at the centre (right image of figure 1). The radius of the hole was 10 mm. The optical properties of the test cases are summarized in table 1. In all of the test cases, the background absorption and scattering coefficients were $\mu_a = 0.025$ mm^{-1} and $\mu_s = 2$ mm^{-1}, respectively, and the absorption coefficient of the hole was $\mu_a = 0.025$ mm^{-1}. In the first test case (case 2.A), the hole consisted of low-scattering medium ($\mu_s = 0.02$ mm^{-1}) and the scattering probability within the background medium and hole was a uniform distribution ($g = 0$). In the second

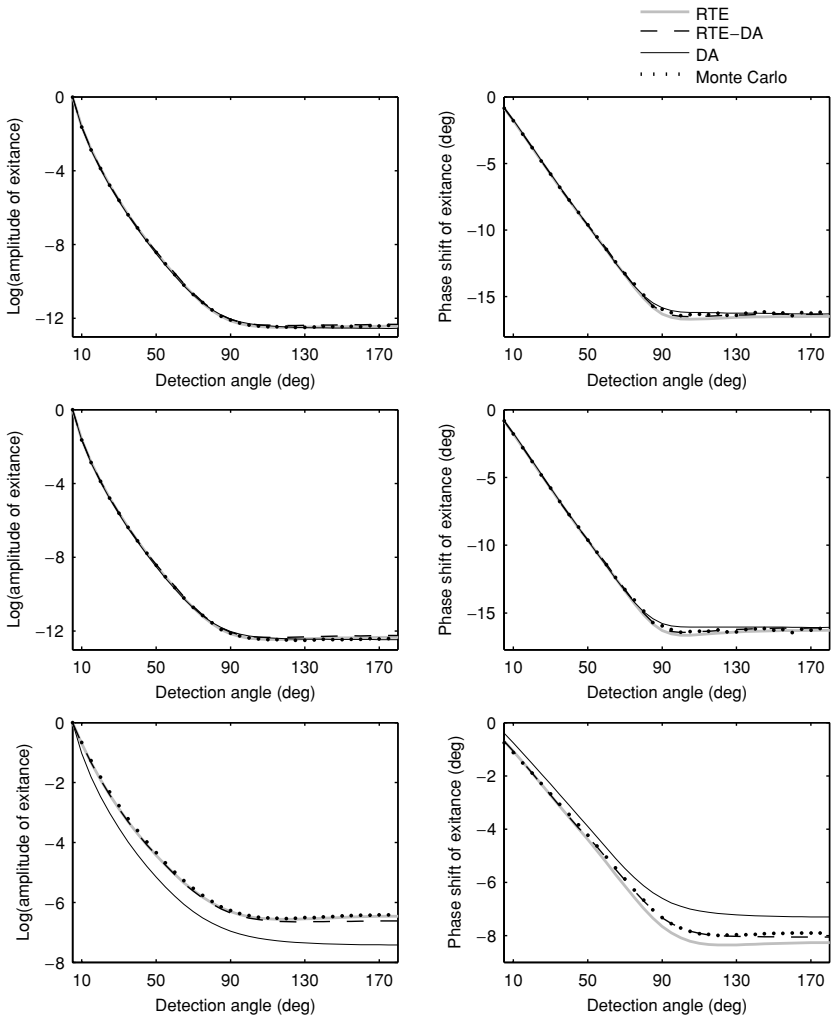

Figure 7. Logarithm of amplitude (left column) and phase shift (right column) of exitance against the detection angle in a domain with a 10 mm radius hole at the centre. From top to bottom: a low-scattering hole (case 2.A), a non-scattering hole (case 2.B) and non-uniform scattering (case 2.C).

test case (case 2.B), the hole consisted of non-scattering medium ($\mu_s = 0$ mm^{-1}) and the scattering probability of the background medium was a uniform distribution ($g = 0$). In the third test case (case 2.C), the hole consisted of low-scattering medium, $\mu_s = 0.02$ mm^{-1}, and the scattering probability was a non-uniform distribution with the background and hole scattering shape parameters $g = 0.8$ and $g = 0.9$, respectively.

The photon densities inside the domain for the low-scattering hole test (case 2.A) are shown in figure 5. The FE-solutions from left to right are the RTE solution, the coupled RTE–DA solution and the DA solution. The logarithms of amplitudes are shown on the top row and the phase shifts are shown on the bottom row. The photon densities along the source direction for all of the test cases are shown in figure 6. The logarithms of amplitudes against the distance from the source are shown on the left, and the phase shifts against the distance

from the source are shown on the right. The images from top to bottom are from the following test cases: a low-scattering hole (case 2.A), a non-scattering hole (case 2.B) and non-uniform scattering (case 2.C) where the optical properties are as shown in table 1. The results in figures 5 and 6 are in the same scale.

The exitances on the boundary of the domain are shown in figure 7. The logarithms of amplitudes against the detection angle are shown on the left, and the phase shifts against the detection angle are shown on the right. The images from top to bottom are from the following test cases: a low-scattering hole (case 2.A), a non-scattering hole (case 2.B) and non-uniform scattering (case 2.C) where the optical properties are as shown in table 1.

Examining the photon densities inside the domain shows again that the photons tend to propagate further within the low-scattering or non-scattering hole. This can clearly be seen from figure 5 in which the logarithms of amplitudes and phase shifts of photon densities inside the domain are shown for the low-scattering hole case. The amplitudes and phase shifts of photon densities obtained with the coupled RTE–DA model are almost equal to the RTE solution. This can be seen from figure 6 in which the photon densities against the distance from the source are shown. The photon densities solved with the DA, however, differ from the RTE solution especially on the location of the hole.

Examining the exitances on the boundary of the domain and comparing the FE-solutions with the Monte Carlo simulations supports the results. The coupled RTE–DA model and the RTE give almost the same results as Monte Carlo. This can be seen from figure 7 in which the logarithms of amplitudes of exitances against the detection angle are shown on the left, and the phase shifts of exitances against the detection angle are shown on the right. As can be seen from figure 7, the DA solution does not show a clear difference from the other approaches when the scattering probability is a uniform distribution ($g = 0$ in cases 2.A and 2.B). However, when $g = 0.8$ and $g = 0.9$ (case 2.C) the DA solution differs from the other approaches.

5. Discussion and conclusions

In this paper, a coupled RTE–DA model was extended for light propagation in turbid medium with low-scattering and non-scattering regions. The RTE is used as a model for light propagation in sub-domains in which the assumptions of the DA are not valid. These sub-domains include the regions in the proximity of the source and boundary and the low-scattering and non-scattering regions. The DA is used as a forward model elsewhere in the domain. The two equations are coupled through their boundary conditions and they are solved simultaneously using the FEM.

The proposed method was tested with 2D simulations in a circular domain. Two types of inclusions were investigated: a ring-like gap close to the boundary and a hole at the centre. Both geometries were tested with different optical properties including low-scattering and non-scattering inclusions. The results of the coupled RTE–DA model were compared with the FE-solutions of the RTE and the DA and with the results of the Monte Carlo simulation.

The results show that in the case of a low-scattering or a non-scattering gap close to the boundary, the coupled RTE–DA model gives almost the same results as the finite element solution of the RTE. Moreover, the FE-solutions of the coupled RTE–DA model and the RTE are similar to the results of the Monte Carlo simulation. The DA solution, however, differs clearly from the other approaches. This is especially evident for the phase data. In the case of the hole at the centre, the coupled RTE–DA model gives almost the same results as the FE-solution of the RTE and the Monte Carlo simulation. The DA solution does not show a clear difference from the other approaches in the cases in which the scattering probability is a

uniform distribution. However, when the scattering probability is a non-uniform distribution, the DA solution differs from the other approaches clearly.

When comparing the memory requirements of the finite element solutions, it should be noted that the FE-discretization of the RTE includes both the spatial and angular discretizations. Thus, compared to the DA with the same spatial FE-discretization, the RTE problem is bigger than the DA problem. The coupled RTE–DA model includes both the RTE and DA sub-domains, and thus the angular discretization is needed in the RTE sub-domain only. This makes the coupled RTE–DA problem smaller than the RTE problem in the whole domain and the computation times are shorter as well. This difference in computational burden is even more significant in larger domains and in the three-dimensional case of DOT where the angular RTE discretization includes both azimuth and zenith angles.

In conclusion, the results show that the coupled RTE–DA model can be used to describe photon migration in turbid medium with low-scattering and non-scattering regions accurately. Further, the results show that the coupled RTE–DA model gives better results than the conventional diffusion model. Furthermore, the FE-discretization of the coupled RTE–DA model can be smaller than the FE-discretization of the RTE in the whole domain, and thus the computation times are shorter as well.

Acknowledgments

This work was supported by the National Technology Agency of Finland (TEKES) contract 40781/00, Academy of Finland (projects 206449, 203985 and 108299), the Jenny and Antti Wihuri Foundation, and EPSRC grant GR/R86201/01. A collaborative travel grant was provided by the Wellcome Trust. The authors wish to thank Antti Vanne for providing a computer cluster environment and algorithms, and Jenni Heino for the assistance with the Monte Carlo simulations.

References

Alexandrakis G, Farrell T and Patterson M 2000 Monte Carlo diffusion hybrid model for photon migration in a two-layer medium in the frequency domain *Appl. Opt.* **39** 2235–44

Arridge S R 1999 Optical tomography in medical imaging *Inverse Problems* **15** R41–R93

Arridge S R, Dehghani H, Schweiger M and Okada E 2000 The finite element model for the propagation of light in scattering media: a direct method for domains with nonscattering regions *Med. Phys.* **27** 252–64

Arridge S R and Hebden J C 1997 Optical imaging in medicine: II. Modelling and reconstruction *Phys. Med. Biol.* **42** 841–53

Bal G and Maday Y 2002 Coupling of transport and diffusion models in linear transport theory *Math. Model. Numer. Anal.* **36** 69–86

Dehghani H, Arridge S R, Schweiger M and Delpy D T 2000 Optical tomography in the presence of void regions *J. Opt. Soc. Am.* A **17** 1659–67

Dorn O 1998 A transport–backtransport method for optical tomography *Inverse Problems* **14** 1107–30

Gibson A P, Hebden J C and Arridge S R 2005 Recent advances in diffuse optical imaging *Phys. Med. Biol.* **50** R1–R43

Hayashi T, Kashio Y and Okada E 2003 Hybrid Monte Carlo–diffusion method for light propagation in tissue with a low-scattering region *Appl. Opt.* **42** 2888–96

Heino J, Arridge S, Sikora J and Somersalo E 2003 Anisotropic effects in highly scattering media *Phys. Rev.* E **68**

Heino J and Somersalo E 2002 Estimation of optical absorption in anisotropic background *Inverse Problems* **18** 559–73

Heiskala J, Nissilä I, Neuvonen T, Järvenpää S and Somersalo E 2005 Modeling anisotropic light propagation in a realistic model of the human head *Appl. Opt.* **44** 2049–57

Henyey L G and Greenstein J L 1941 Diffuse radiation in the galaxy *Astrophys. J.* **93** 70–83

Kaipio J and Somersalo E 2005 *Statistical and Computational Inverse Problems* (New York: Springer)

Kim A and Keller J 2003 Light propagation in biological tissue *J. Opt. Soc. Am.* A **20** 92–8

Klose A, Netz U, Beuthan J and Hielscher A 2002 Optical tomography using the time-independent equation of radiative transfer: Part 1. Forward model *J. Quant. Spectrosc. Radiat. Transfer* **72** 691–713

Lathrop K D 1968 Ray effects in discrete ordinates equations *Nucl. Sci. Eng.* **32** 357–69

Lathrop K D 1971 Remedies for ray effects *Nucl. Sci. Eng.* **45** 255–68

Prahl S, Keijzer M, Jacques S and Welch A 1989 A Monte Carlo model of light propagation in tissue *SPIE Proc. Dosimetry of Laser Radiation in Medicine and Biology* ed G Müller and D Sliney vol IS 5, pp 102–11

Richling S, Meinköhn E, Kryzhevoi N and Kanschat G 2001 Radiative transfer with finite elements: I. Basic method and tests *Astron. Astrophys.* **380** 776–88

Schweiger M, Arridge S R, Hiraoka M and Delpy D T 1995 The finite element model for the propagation of light in scattering media: boundary and source conditions *Med. Phys.* **22** 1779–92

Tarvainen T, Vauhkonen M, Kolehmainen V and Kaipio J P 2005a Hybrid radiative–transfer–diffusion model for optical tomography *Appl. Opt.* **44** 876–86

Tarvainen T, Vauhkonen M, Kolehmainen V and Kaipio J P 2005b Finite element model for the coupled radiative transfer equation and diffusion approximation *Int. J. Numer. Methods Eng.* at press (doi: 10.1002/nme.1451)

Wang L and Jacques S L 1993 Hybrid model of Monte Carlo simulation and diffusion theory for light reflectance by turbid media *J. Opt. Soc. Am.* A **10** 1746–52